Earth Syst. Sci. Data, 18, 8903–8921, 2026
https://doi.org/10.5194/essd-18-8903-2026
© Author(s) 2026. This work is distributed under
the Creative Commons Attribution 4.0 License.

Open Access Earth System Science Data

GIFT-BDS: a high-resolution TEC and Gradient Ionospheric Index dataset over China derived from BeiDou GEO fixed-geometry observations

Zhiyao Li[1], Jiahao Zhong[1], Ningbo Wang[2], Yongqiang Hao[1], Yunbin Yuan[3], Norbert Jakowski[4], Mohammed Mainul Hoque[4], Ang Liu[2], Zishen Li[2], and Xin Wan[1]

[1]Planetary Environmental and Astrobiological Research Laboratory (PEARL), School of Atmospheric Sciences, Sun Yat-sen University, Zhuhai, China
[2]Aerospace Information Research Institute (AIR), Chinese Academy of Sciences (CAS), Beijing, China
[3]State Key Laboratory of Precision Geodesy, Innovation Academy for Precision Measurement Science and Technology, Chinese Academy of Sciences, Wuhan, China
[4]Institute for Solar-Terrestrial Physics, German Aerospace Center (DLR), Neustrelitz, Germany

Correspondence: Ningbo Wang (wangningbo@aoe.ac.cn)

Received: 6 July 2026 – Discussion started: 31 August 2026
Revised: 15 October 2026 – Accepted: 11 November 2026 – Published: 25 November 2026

Abstract. High-resolution ionospheric total electron content (TEC) gradient observations are well-suited for characterizing ionospheric spatial structure and for assessing ionospheric effects on Global Navigation Satellite System (GNSS) positioning applications. Existing global ionospheric products provide valuable information on large-scale ionospheric conditions, but their spatial and temporal sampling is generally not sufficient to resolve fine-scale TEC gradient structures over China. We present GIFT-BDS (Gradient Ionospheric index from Fixed-geometry TEC observations using BDS GEO satellites), a high-resolution regional ionospheric dataset derived from a dense ground-based GNSS network and BeiDou geostationary Earth orbit (GEO) fixed-geometry observations. The network consists of more than 200 ground-based GNSS receivers and five BeiDou GEO satellites, providing stable receiver-satellite geometries and repeated sampling of nearly fixed ionospheric pierce points. The released dataset contains two product levels. Level-1 provides 30 s GEO-derived slant TEC (STEC) time series for individual receiver-satellite links. Level-2 provides gridded vertical TEC (VTEC), rate of TEC index (ROTI), Gradient Ionospheric Index (GIX), and directional TEC gradient components. The TEC-gradient products are provided on a $0.25° \times 0.25°$ grid with a temporal resolution of 15 min. The dataset is assessed using STEC stability statistics, internal consistency diagnostics, and comparison with Global Ionospheric Map (GIM)-derived gradients. Selected examples illustrate the use of GIFT-BDS for studies of daytime Equatorial Ionization Anomaly (EIA) morphology, nighttime Equatorial Plasma Bubble (EPB) evolution, and ionospheric effects on Precise Point Positioning (PPP) and Real-Time Kinematic (RTK) positioning performance. The dataset is available at https://doi.org/10.5281/zenodo.21090695 (Li et al., 2026a), with operational updates provided at https://data.bdsmart.cn/pub/campaign/iono/ (last access: 23 November 2026). GIFT-BDS extends the currently available ionospheric data resources over China by providing continuous high-resolution observations of TEC and TEC gradients, enabling investigations of ionospheric dynamics, space-weather effects, and GNSS positioning error characterization.

Published by Copernicus Publications.

1 Introduction

High-resolution ionospheric observations are required to describe regional electron-density structures and to assess their impact on trans-ionospheric radio signals. The ionosphere affects Global Navigation Satellite System (GNSS) signals through propagation delay caused by spatially variable total electron content (TEC), making it one of the main error sources for positioning, navigation and timing (PNT) applications. Beyond its practical relevance for GNSS, ionospheric variability provides information on geospace processes driven by solar-terrestrial forcing, geomagnetic activity, and neutral-atmosphere dynamics (Buonsanto, 1999; Francis, 1974; Hedin, 1987; Sheng et al., 2025). Spatially dense and temporally continuous regional observations are therefore needed to characterize ionospheric structures and associated TEC gradients, particularly in regions where low- and mid-latitude processes coexist.

The Chinese sector spans low- and mid-latitude ionospheric regions and exhibits variability over a wide range of spatial and temporal scales. Daytime Equatorial Ionization Anomaly (EIA) development and nighttime Equatorial Plasma Bubble (EPB) activity are two representative manifestations of low-latitude ionospheric variability in this sector (Balan et al., 2018; Li et al., 2021a). These phenomena reflect both the background electrodynamic evolution of the low-latitude ionosphere and the development of plasma instabilities, with clear local-time, seasonal and regional dependences (Abdu, 2001; Chen et al., 2016; Li et al., 2021a). Geomagnetic storms may further produce strong regional responses through the coupled effects of solar-wind forcing, geomagnetic activity, and thermosphere–ionosphere dynamics (Chen et al., 2025; Zhang et al., 2024). Atmospheric waves generated by earthquakes and volcanic eruptions can also disturb the ionosphere over broad areas (Astafyeva, 2019; Li et al., 2025a; Zhai et al., 2025). Resolving these structures and their associated TEC gradients requires observations with sufficient spatial sampling and temporal continuity, which are also relevant for assessing ionospheric effects on GNSS-based applications over China (Yang et al., 2021; Yuan et al., 2019).

GNSS observations provide continuous measurements of path-integrated electron density along satellite-receiver lines of sight, and ground-based receiver networks have become an important basis for ionospheric monitoring. Global Ionospheric Maps (GIMs) are among the most widely used public GNSS-based ionospheric products and provide valuable information on large-scale ionospheric background conditions and storm-time responses at global and continental scales (Astafyeva et al., 2015; Chen et al., 2017; Li et al., 2021b). Their spatial and temporal sampling, however, is often not adequate for resolving fine-scale regional TEC gradient structures (Hu et al., 2024; Liu et al., 2026). High-resolution regional products therefore require dense and continuously operated GNSS receiver networks. At the global scale, the International GNSS Service (IGS) provides a widely used network of permanent GNSS stations and openly available ionospheric products (Hernández-Pajares et al., 2009; Liu et al., 2021). At the regional scale, dense GNSS infrastructures, including NOAA CORS, GEONET, EUREF, and Australian GNSS networks, provide important observational bases for regional ionospheric monitoring (Kenyeres and Bruyninx, 2004; Snay and Soler, 2008; Takamatsu et al., 2023; Woodgate et al., 2017). For the China region, GIFT-BDS uses a dedicated ground-based GNSS receiver network comprising more than 200 stations and fixed-geometry observations from BeiDou geostationary Earth orbit (GEO) satellites. In contrast to conventional medium Earth orbit (MEO) GNSS observations, which involve moving line-of-sight (LOS) geometry, BeiDou GEO observations provide nearly fixed receiver-satellite geometry over China. This property enables repeated sampling of nearly fixed ionospheric pierce points and supports temporally consistent regional TEC gradient estimation (Li et al., 2023).

The GIFT-BDS dataset is based on a fixed-geometry ionospheric observation network comprising ground-based GNSS receivers and BeiDou GEO satellites. The near-stationary GEO geometry provides continuous observations over nearly fixed ionospheric pierce points (IPPs), while pairs of IPPs define geometry-invariant inter-IPP vectors on the ionospheric shell (Li et al., 2025b). Each inter-IPP vector is used as a sensing element for estimating VTEC differences mapped to the ionospheric shell over a known distance. This configuration increases the spatial sampling density and redundancy of regional gradient observations without relying on moving IPP tracks (Jakowski and Hoque, 2019). Spatial TEC gradients are derived from the network of inter-IPP vectors, whereas temporal TEC variations are estimated from the time series at nearly fixed IPPs. The same observation geometry therefore supports the generation of both Level-1 GEO-derived slant TEC (STEC) records and Level-2 gridded regional TEC-gradient products.

GEO-derived STEC records and TEC-gradient products are useful for studies of multi-scale ionospheric variability and for analyses of ionospheric effects on GNSS positioning. The nearly fixed LOS geometry supports temporally continuous comparisons at nearly fixed IPPs and reduces sampling differences caused by moving satellite geometry. GEO-based observations have been used, for example, to detect traveling ionospheric disturbances (TIDs) and to estimate the altitude and zonal drift velocity of ionospheric irregularities (Huang et al., 2025; Rao et al., 2025; Zhong et al., 2023). TEC gradients describe horizontal spatial changes in TEC and provide diagnostics of regional ionospheric structure. The Gradient Ionospheric Index (GIX), derived from TEC spatial gradients, is included in the dataset as a quantitative indicator of gradient intensity (Jakowski and Hoque, 2019; Nykiel et al., 2024). Such gradient information can support studies of Equatorial Ionization Anomaly (EIA) evolution, Equatorial Plasma Bubble (EPB) development, and Large-

scale Traveling Ionospheric Disturbance (LSTID) propagation (Fu et al., 2025a; Li et al., 2025b), as well as the analysis of Precise Point Positioning (PPP) and Real-Time Kinematic (RTK) performance under disturbed ionospheric conditions (Fu et al., 2025b; Nykiel et al., 2024). These applications motivate the release of a documented and reusable regional dataset rather than isolated event-based products.

This paper describes GIFT-BDS (Gradient Ionospheric index from Fixed-geometry TEC observations using BeiDou GEO satellites), a high-resolution regional ionospheric TEC and Gradient Ionospheric Index dataset over China. The focus is on dataset construction, product definition, quality control, technical assessment, and example uses. The following sections first describe the ground and space segments of the fixed-geometry observation network. We then present the processing workflow, including GEO-derived STEC generation, TEC gradient estimation, grid mapping, and product standardization. The dataset is assessed using STEC stability statistics, internal consistency diagnostics of the gradient products, and comparison with GIM-derived gradients. Selected examples illustrate representative uses of the dataset for ionospheric process studies and GNSS positioning-related analyses. Finally, data access, usage information, and the operational update procedure are provided.

2 Observation network

The GIFT-BDS dataset is generated from a fixed-geometry ionospheric observation network that combines a dense ground-based GNSS receiver network with BeiDou GEO satellites. The ground segment provides continuous multi-GNSS measurements over China, whereas the GEO satellites provide near-stationary receiver-satellite viewing geometries and repeated sampling of nearly fixed ionospheric pierce points.

2.1 China real-time multi-GNSS station network

The ground segment of GIFT-BDS is the China real-time multi-GNSS station network, which comprises more than 200 continuously operating GNSS stations over China. Each station is equipped with a Septentrio PolaRx5 receiver supporting GPS, GLONASS, Galileo, and BeiDou observations. The stations provide 1 Hz RTCM real-time data streams and 30 s RINEX observation files to the data center. The station network was completed in mid-2024 and has been continuously operated since then. Figure 1 shows the geographical distribution of the receivers within the study region of 15–50° N and 95–135° E. The stations are mainly distributed over the low- and mid-latitude regions of China, with relatively dense and homogeneous coverage south of 35° N. In this southern part of the network, the median nearest-station spacing is approximately 100 km, as shown in Fig. 1b.

Table 1. BeiDou GEO satellites used in the space segment of the GIFT-BDS observation network.

PRN	Satellite	Longitude	Launch Date	Inclination (°)
C01	BDS2 GEO8	144.5° E	17 May 2019	0.4001
C02	BDS2 GEO6	84.0° E	25 Oct 2012	1.4764
C03	BDS2 GEO7	110.5° E	12 Jun 2016	1.5196
C04	BDS2 GEO4	160.0° E	31 Oct 2010	0.8047
C05	BDS2 GEO5	59.0° E	24 Feb 2012	1.8963

2.2 BeiDou GEO satellites

The space segment of the GIFT-BDS observation network consists of five GEO satellites from the BeiDou Navigation Satellite System (BDS). Table 1 lists the PRN identifier, satellite name, nominal longitude, launch date, and orbital inclination of each BeiDou GEO satellite used in the processing. The five GEO satellites are located at different longitudes and therefore provide multiple fixed-viewing geometries over the China region. Unlike MEO GNSS satellites, BeiDou GEO satellites provide near-stationary receiver-satellite geometry. Each valid receiver-GEO link defines a line of sight and an associated IPP on the assumed ionospheric shell. These IPPs vary only slowly with time, enabling repeated sampling of nearly the same ionospheric regions.

2.3 Input data and auxiliary products

Based on the observation network described in Sect. 2.1 and 2.2, the GIFT-BDS dataset generation uses archived station observation files together with several auxiliary products. The daily RINEX observation files provide the primary ground-based input. These files are archived at an internal data center with a sampling interval of 30 s. The station coordinate file provides receiver positions for geometric calculations. Broadcast ephemerides supply satellite orbit information for the BeiDou GEO satellites. Satellite code bias products are used for satellite DCB corrections, and IONEX products provide a global ionospheric background used in receiver bias estimation. The detailed processing steps are described in Sect. 3. The combined information is summarized in Table 2.

3 Data processing and product generation

The GIFT-BDS dataset is organized into two product levels. Level-1 contains 30 s GEO-derived STEC time series for individual receiver-satellite links, together with rate of TEC index (ROTI), LOS geometry and IPP information. These observation-level records form the basis for the higher-level gridded products. Level-2 provides gridded VTEC, ROTI and TEC-gradient variables derived from Level-1 products.

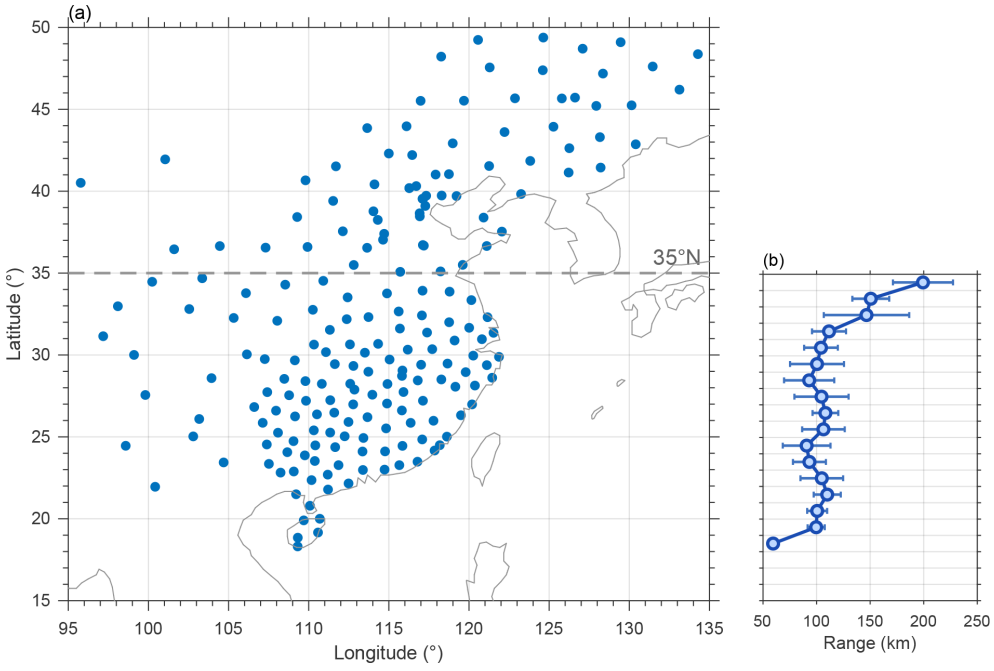


Figure 1. Ground segment of the GIFT-BDS observation network. **(a)** Geographical distribution of the China real-time multi-GNSS station network over the study region (15–50° N, 95–135° E). **(b)** Median nearest-station spacing within 1° latitude bins south of 35° N. The horizontal dashed line in **(a)** denotes 35° N.

Table 2. Essential input data and auxiliary products used for GIFT-BDS dataset generation.

Data	Institution	URL
Daily RINEX observation files	China real-time multi-GNSS station network	–
Station coordinate file	Network coordinate solution	–
Multi-GNSS broadcast ephemeris	IGS	`ftp://igs.ign.fr/pub/igs/data/yyyy/ddd/BRDC00IGS_R_yyyyddd0000_01D_MN.rnx.gz`
Satellite code bias product	CAS	`https://data.bdsmart.cn/pub/product/bias/yyyy/CAS0MGXRAP_yyyyddd0000_01D_01D_DCB.BSX.gz`
IONEX product	UPC	`https://data.bdsmart.cn/pub/product/iono/ionex/yyyy/ddd/uqrgddd0.yyi.Z`

The spatial gradient fields are provided on a $0.25° \times 0.25°$ grid to describe regional ionospheric variability over China at a finer spatial scale. Figure 2 shows the two-stage processing workflow used to generate the released GIFT-BDS dataset from raw BeiDou GEO observations. The Level-1 processing uses raw GEO measurements and auxiliary GNSS products to estimate DCB-corrected STEC time series and the associated LOS geometry for each receiver-satellite link. The resulting STEC and geometry records are then used in the Level-2 processing, where regional TEC, ROTI and TEC-gradient quantities are derived and mapped onto regular grids. Details of the individual processing steps are given in the following subsections.

3.1 Level-1 dataset generation

3.1.1 GEO-derived STEC

For each GEO satellite-receiver link, the GEO-derived STEC time series is generated from dual-frequency carrier-phase observations using the B1I/B3I geometry-free combination at a sampling interval of 30 s. The B1I and B3I signals correspond to carrier frequencies of 1561.098 and 1268.52 MHz,

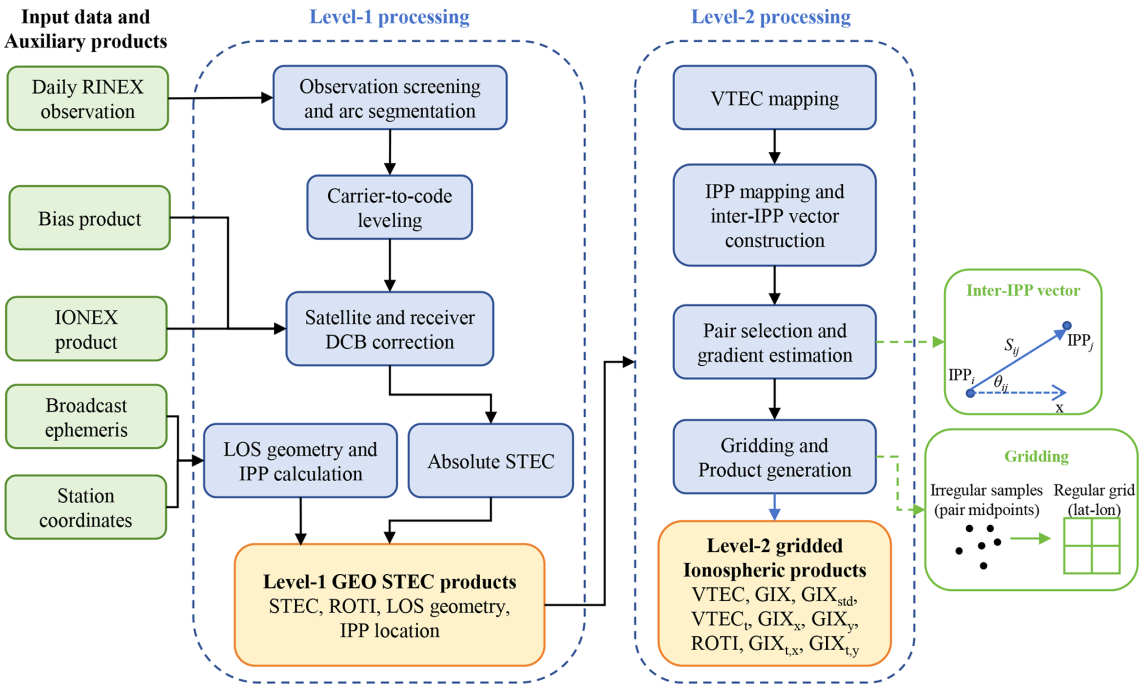


Figure 2. Two-stage processing workflow used to generate the GIFT-BDS Level-1 and Level-2 ionospheric products.

respectively (Li et al., 2026b). Observations with elevation angles below 20° are excluded to reduce multipath effects and low-elevation geometry-related errors. The carrier-phase geometry-free combination can be converted to STEC as:

$$T_S = \frac{{f_1}^2 {f_2}^2}{40.3 \times 10^{16}({f_1}^2 - {f_2}^2)}\big[(\lambda_1 L_1 - \lambda_2 L_2) - (\lambda_1 N_1 - \lambda_2 N_2) + (d_1 - d_2)\big] \quad (1)$$

where T_S denotes the STEC in TECU (1 TECU = 10^{16} electrons m^{-2}), L_1 and L_2 are the carrier-phase measurements in cycles at two frequencies f_1 and f_2, respectively, λ_1 and λ_2 are the corresponding wavelengths, N_1 and N_2 are the integer ambiguities, and d_1 and d_2 are the frequency-dependent hardware delays. The ambiguity-related term remains constant within a continuous carrier-phase arc and is absorbed into an arc-dependent leveling offset.

Level-1 processing is performed independently for each receiver-satellite link. After applying the elevation mask, cycle slips and data gaps are detected from the geometry-free phase combination, and the observations are segmented into continuous arcs. Within each arc, the precise but ambiguous carrier-phase STEC is aligned with the code-derived STEC by carrier-to-code leveling (CCL; Mannucci et al., 1998). This procedure removes the arc-dependent ambiguity offset while preserving the high precision of the carrier-phase observations. The processing system obtains satellite code biases from the daily CAS BSX bias products provided by the Chinese Academy of Sciences (CAS, Wang et al., 2016, 2026). Level-1 processing estimates receiver DCBs from dual-frequency code observations using the GIM listed in Table 2 as the a priori ionospheric background, following the general GIM-assisted approach (Montenbruck et al., 2014). The estimated receiver DCBs and CAS satellite DCBs are then applied in the carrier-to-code leveling of the STEC observations. Therefore, the released Level-1 STEC records are corrected for both satellite and receiver code biases.

Residual DCB errors remain in both satellite and receiver bias corrections. The external satellite DCB products contain errors from the underlying bias solutions, while the receiver DCB estimates depend on the accuracy of the a priori GIM. Previous studies report receiver DCB consistency at the level of several tenths of a nanosecond (Li et al., 2018; Wang et al., 2016). For the B1I/B3I combination used here, several tenths of a nanosecond correspond to an STEC effect on the order of 1 TECU. Additional receiver DCB errors may arise when regional ionospheric structures are not adequately represented by the relatively coarse GIM. These residual DCB errors mainly affect the absolute STEC level.

3.1.2 Quality control

Quality control is implemented at the epoch, arc, and LOS levels. At the epoch and arc levels, elevation screening, cycle-slip detection, data-gap identification, and continuous-arc segmentation are applied to define valid carrier-phase arcs for each receiver-satellite link (Kim et al., 2014). These procedures use the same settings under quiet and

disturbed ionospheric conditions. Strong disturbances may cause signal interruptions or loss of lock, resulting in gaps in the carrier-phase observations and reduced data availability. Carrier-to-code leveling and DCB corrections are then applied to these valid arcs to generate absolute STEC time series. To avoid retaining receiver-satellite links with persistently unstable behavior, the overall stability of each LOS STEC record is further checked using a detrended STEC residual. The residual is computed using a 5 min moving window (Ma et al., 2022):

$$\mathrm{STEC}_{\mathrm{res}}(t) = \mathrm{STEC}(t) - \overline{\mathrm{STEC}}_{5\,\mathrm{min}}(t) \tag{2}$$

where $\overline{\mathrm{STEC}}_{5\,\mathrm{min}}(t)$ denotes the moving-average STEC within the 5 min window centered at epoch t. The residual series $\mathrm{STEC}_{\mathrm{res}}(t)$ is used as a LOS-level stability indicator. This criterion is evaluated separately for each daily receiver-satellite LOS. A daily receiver-satellite LOS is excluded if the mean absolute residual during quiet ionospheric periods (ROTI < 0.3 TECU min^{-1}) exceeds 0.15 TECU. The 0.15 TECU threshold is applied to the daily LOS and not to individual high-ROTI epochs. This criterion is used to remove links with persistently unstable residual behavior, which may be caused by receiver-related problems or unstable observations. The retained LOS STEC records are used to form the released Level-1 product and provide the observational basis for the Level-2 products.

3.1.3 Released Level-1 products

The Level-1 products are released as time series for individual receiver-GEO satellite links. Each time series corresponds to one valid LOS at a 30 s sampling interval and contains the GEO-derived STEC, the corresponding ROTI, and the associated elevation angle and IPP information. These variables provide the direct observational basis for the Level-2 gridded products. The main variables released in the Level-1 products are summarized in Table 3.

3.2 Level-2 dataset generation

The Level-2 products are generated from the quality-controlled Level-1 STEC products. This product level includes gridded VTEC, ROTI, temporal TEC gradients at fixed IPPs, and horizontal TEC-gradient quantities from inter-IPP vectors. The following subsections describe the processing steps used to derive these variables.

3.2.1 GEO-derived ROTI

The LOS-level ROTI is first computed from the Level-1 STEC series and then mapped onto the Level-2 grid. The ROTI describes short-term fluctuations in the rate of TEC change (ROT) and characterizes ionospheric irregularity activity (Li et al., 2026b; Zhang et al., 2025). In GIFT-BDS, ROTI is computed for each valid receiver-satellite link over a 5 min moving window as (Pi et al., 1997):

$$I^i_{\mathrm{ROTI}} = \sqrt{\left\langle \left(I^i_{\mathrm{ROT}}\right)^2 \right\rangle - \left\langle I^i_{\mathrm{ROT}} \right\rangle^2} \tag{3}$$

where I^i_{ROTI} denotes the ROTI value at IPP i, and $\langle\cdot\rangle$ denotes averaging over the 5 min window. The corresponding I^i_{ROT} is defined as:

$$I^i_{\mathrm{ROT}} = \frac{\Delta T^i_{\mathrm{S}}}{\Delta t} = \frac{T^i_{\mathrm{S}}(t_2) - T^i_{\mathrm{S}}(t_1)}{t_2 - t_1} \tag{4}$$

where $T^i_{\mathrm{S}}(t_1)$ and $T^i_{\mathrm{S}}(t_2)$ are the STEC values at two epochs, and $\Delta t = 0.5$ min (30 s).

3.2.2 VTEC and temporal derivative estimation at fixed IPPs

STEC at each receiver-satellite link is mapped to VTEC using the elevation-dependent mapping function. A single-layer ionospheric shell model is adopted with a fixed shell height of 400 km (Klobuchar, 1987; Zhong et al., 2016a). The mapping function $M(\delta)$ is written as:

$$M(\delta) = \frac{1}{\sqrt{1 - \left(\frac{R_{\mathrm{e}}\cos\delta}{R_{\mathrm{e}}+h}\right)^2}} \tag{5}$$

where R_{e} is the Earth's radius, h is the ionospheric shell height, and δ is the satellite elevation angle. The VTEC at IPP i is then obtained as:

$$T^i_{\mathrm{V}} = \frac{T^i_{\mathrm{S}}}{M\left(\delta^i\right)} + \frac{\xi^i}{M\left(\delta^i\right)} \tag{6}$$

where T^i_{S} is the Level-1 STEC, and $\frac{\xi^i}{M(\delta^i)}$ represents the mapped residual uncertainty in the VTEC estimation. The residual term includes contributions from measurement noise, multipath effects, mapping-function approximation errors, and residual satellite and receiver DCB errors. Previous TEC calibration and GIX error analyses indicate that the residual link-related TEC bias after calibration is typically on the order of 1 TECU (Montenbruck et al., 2014; Jakowski et al., 2026). This residual bias directly affects the absolute VTEC level. Its contribution to the derived TEC gradients depends on the spatial differencing geometry, as discussed in Sect. 3.2.4 (Jakowski and Hoque, 2019; Jakowski et al., 2026).

The temporal derivative of VTEC at IPP i is derived from the STEC rate of change. Because the receiver-GEO LOS geometry varies slowly over short time intervals, the mapping function can be treated as locally stable for the 30 s ROT calculation (Li et al., 2023; Zhong et al., 2016b). The VTEC temporal derivative is therefore approximated as:

$$\frac{\partial T^i_{\mathrm{V}}}{\partial t} = \frac{1}{M\left(\delta^i\right)}\frac{\Delta T^i_{\mathrm{S}}}{\Delta t} = \frac{1}{M\left(\delta^i\right)} I^i_{\mathrm{ROT}} \tag{7}$$

Table 3. Summary of Level-1 variables released in the GIFT-BDS dataset.

Variable	Description	Unit
STEC	GEO-derived slant TEC along the receiver-satellite LOS	TECU
ROTI	Rate of TEC index derived from the STEC time series	TECU min^{-1}
Elevation angle	Satellite elevation angle at the receiver	degree
IPP latitude	Latitude of the IPP on the ionospheric shell at 400 km	degree
IPP longitude	Longitude of the IPP on the ionospheric shell at 400 km	degree
LOS ID	Identifier of the receiver-satellite LOS	–

where I^{i}_{ROT} is the STEC rate of change defined in Eq. (4).

3.2.3 Spatial gradient estimation from inter-IPP vectors

Spatial-gradient products are derived from pairs of simultaneous IPP observations. For two IPPs, i and j, a directed inter-IPP vector from IPP i to IPP j is constructed on the ionospheric thin shell. Its magnitude $S^{(i,j)}$ is the great-circle distance between the two IPPs, and its azimuth angle $\theta^{(i,j)}$ is measured clockwise from north. Due to the near-stationary GEO observation geometry, both $S^{(i,j)}$ and $\theta^{(i,j)}$ vary only slowly with time. The signed TEC spatial gradient along the directed inter-IPP vector is estimated as:

$$g_{\mathrm{V}}^{(i,j)}(t) \equiv \frac{\partial T_{\mathrm{V}}^{(i,j)}}{\partial S^{(i,j)}}\Big|_{t} = \frac{T_{\mathrm{V}}^{j}(t) - T_{\mathrm{V}}^{i}(t)}{S^{(i,j)}} \tag{8}$$

Substituting Eq. (6) into Eq. (8) gives:

$$g_{\mathrm{V}}^{(i,j)}(t) = \left(\frac{T_{\mathrm{S}}^{j}}{M\left(\delta^{j}\right)} - \frac{T_{\mathrm{S}}^{i}}{M\left(\delta^{i}\right)}\right) \cdot \frac{1}{S^{(i,j)}} + \frac{1}{S^{(i,j)}} \cdot \left(\frac{\xi^{j}}{M\left(\delta^{j}\right)} - \frac{\xi^{i}}{M\left(\delta^{i}\right)}\right) \tag{9}$$

A positive value of $g_{\mathrm{V}}^{(i,j)}$ indicates that VTEC increases from IPP i toward IPP j. The unsigned magnitude of the spatial TEC gradient along the inter-IPP vector is defined as:

$$\nabla T_{\mathrm{V}}^{(i,j)}(t) = \left| g_{\mathrm{V}}^{(i,j)}(t) \right| \tag{10}$$

and is used as the GIX. The corresponding signed zonal (x) and meridional (y) components are given by:

$$\frac{\partial T_{\mathrm{V}}^{(i,j)}}{\partial x}\Big|_{t} = g_{\mathrm{V}}^{(i,j)}(t)\sin\theta^{(i,j)} \tag{11}$$

$$\frac{\partial T_{\mathrm{V}}^{(i,j)}}{\partial y}\Big|_{t} = g_{\mathrm{V}}^{(i,j)}(t)\cos\theta^{(i,j)} \tag{12}$$

The signed $g_{\mathrm{V}}^{(i,j)}$ preserves the direction of TEC increase in both components. Positive x and y denote the eastward and northward directions, respectively.

The spatial variation of the temporal VTEC gradient is derived from the difference in temporal derivatives between the two IPPs:

$$\frac{\partial^{2} T_{\mathrm{V}}^{(i,j)}}{\partial x\,\partial t} = \left(\frac{\partial T_{\mathrm{V}}^{j}}{\partial t} - \frac{\partial T_{\mathrm{V}}^{i}}{\partial t}\right) \cdot \frac{\sin\theta^{(i,j)}}{S^{(i,j)}} \tag{13}$$

$$\frac{\partial^{2} T_{\mathrm{V}}^{(i,j)}}{\partial y\,\partial t} = \left(\frac{\partial T_{\mathrm{V}}^{j}}{\partial t} - \frac{\partial T_{\mathrm{V}}^{i}}{\partial t}\right) \cdot \frac{\cos\theta^{(i,j)}}{S^{(i,j)}} \tag{14}$$

In practice, each inter-IPP gradient estimate is assigned to the midpoint of the great-circle arc connecting IPPs i and j. This midpoint is used as the representative location of the gradient sample in the subsequent gridding procedure.

3.2.4 Quality control and pair-selection strategy

The uncertainty of the spatial gradient estimates originates from the residual errors in the individual VTEC observations at each IPP, including measurement noise, multipath effects, mapping-function approximation errors, and residual satellite and receiver DCB errors. According to Eq. (9), the contribution of residual VTEC errors to the gradient estimate decreases as the inter-IPP distance increases. Specifically, short inter-IPP distances may amplify residual observation errors because the spatial difference is normalized by a smaller separation. Differences in mapping factors between the two line-of-sight observations may introduce additional non-common projection errors. The pair-selection strategy therefore constrains both the inter-IPP distance and the mapping-factor difference.

In the Level-2 processing, only selected inter-IPP pairs are retained. Three constraints are applied. First, the inter-IPP distance $S^{(i,j)}$ must exceed 50 km to limit error amplification at short baselines. Second, $S^{(i,j)}$ must be smaller than 1000 km to limit spatial averaging of smaller-scale TEC structures at long baselines. Third, the difference in mapping-function values between the two IPPs, $\Delta M = \left|M\left(\delta^{j}\right) - M\left(\delta^{i}\right)\right|$, must be smaller than 0.2 (Jakowski and Hoque, 2019). These criteria account for both the error propagation in the TEC-gradient estimate and the spatial sampling characteristics of BeiDou GEO fixed-geometry observations. The pair selection is applied epoch by epoch. The retained inter-IPP vectors form the basis of the spatial-gradient products. Because the BeiDou GEO viewing geometry changes only slowly, the valid pair geometry is generally stable in time, except during data gaps, station outages,

and quality-control exclusions. This temporal stability supports the generation of temporally continuous regional TEC-gradient products.

The inter-IPP distance range determines the spatial scale of the TEC-gradient estimates. Figure 3 illustrates this dependence using Level-1 GEO observations grouped by inter-IPP distance. The absolute VTEC difference increases steadily with distance, whereas the corresponding gradient magnitude decreases (Fig. 3a, b). The increasing VTEC difference indicates that longer baselines sample TEC variations over broader spatial regions. At short baselines, the P95 gradient decreases rapidly with increasing distance, reflecting the combined effects of greater sensitivity to residual observation errors and localized ionospheric variability. At larger separations, the median gradient decreases more gradually and the gradient distribution becomes narrower, consistent with increasing spatial averaging of smaller-scale TEC structures. The influence of the upper distance threshold was further examined by increasing the maximum inter-IPP distance from 500 to 1000 km. The mean gradient magnitude over all retained pairs decreases from 0.0513 to 0.0451 TECU km^{-1}, corresponding to a reduction of approximately 12.2 %. This difference quantifies the sensitivity of the derived gradient magnitude to the adopted upper distance threshold and is consistent with increased spatial averaging at longer baselines. The adopted 50–1000 km range represents a compromise between limiting error amplification at short baselines and avoiding excessive spatial averaging at long baselines. The Level-1 STEC observations and IPP geometry are also provided, allowing users to derive gradients over alternative baseline ranges when required.

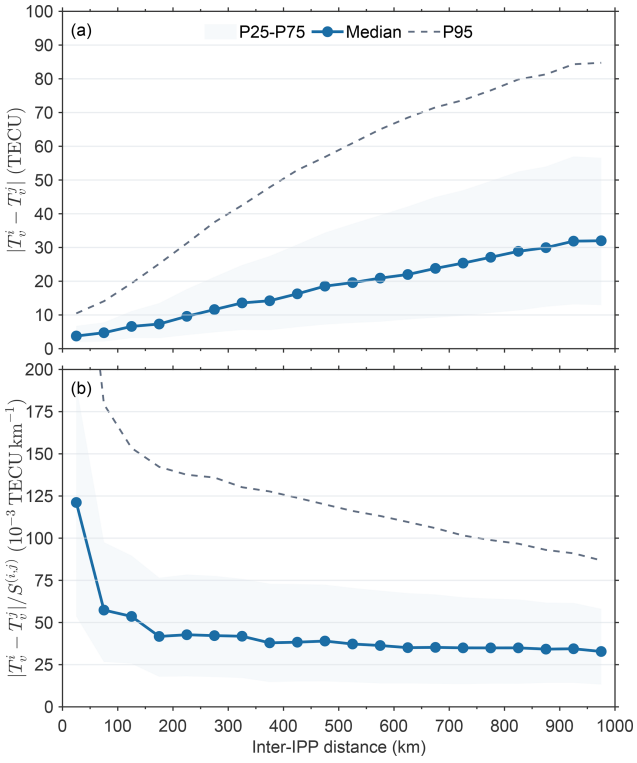


Figure 3. Dependence of pairwise VTEC differences and TEC-gradient estimates on inter-IPP distance. **(a)** Absolute VTEC difference, $\left|T_{\mathrm{V}}^i - T_{\mathrm{V}}^j\right|$. **(b)** VTEC gradient, $\left|T_{\mathrm{V}}^i - T_{\mathrm{V}}^j\right|/S^{(i,j)}$, where $S^{(i,j)}$ denotes the inter-IPP distance. BDS GEO Level-1 data were sampled at 15 min intervals from 05:20 to 08:20 UT on 21 September 2024. A total of 861 247 valid pairs satisfying $\Delta M < 0.2$ were grouped into 50 km distance bins according to inter-IPP distance. Inter-IPP distances below the 50 km lower limit were included to characterize the short-baseline behavior. Solid lines indicate the medians, shaded regions denote the P25–P75 intervals, and dashed lines indicate the P95 values.

3.2.5 Gridding and released Level-2 products

The Level-2 products are released as gridded regional ionospheric products. All Level-2 products have a temporal resolution of 15 min. They are generated at 15 min intervals from 00:00 to 23:45 UTC using the Level-1 records at the corresponding 30 s epochs. The Level-2 time-tag corresponds to the sampling epoch. The released Level-2 dataset includes the following variables: VTEC, VTEC$_t$, ROTI, GIX, GIX$_{\mathrm{std}}$, GIX$_x$, GIX$_y$, GIX$_{\mathrm{t},x}$, and GIX$_{\mathrm{t},y}$. Their spatial resolutions, units, and source quantities are summarized in Table 4. The IPP-based variables, including VTEC, ROTI, and the temporal derivative $\frac{\partial T_{\mathrm{V}}}{\partial t}$, are mapped onto a $1^\circ \times 1^\circ$ grid according to the IPP locations. The inter-IPP-based variables, including GIX, GIX$_x$, GIX$_y$, GIX$_{\mathrm{t},x}$, and GIX$_{\mathrm{t},y}$, are mapped onto a $0.25^\circ \times 0.25^\circ$ grid according to the inter-IPP vector midpoints. The value in each grid cell is calculated as the arithmetic mean of all valid samples within that cell. Missing or quality-controlled Level-1 records are omitted.

At each output epoch, a grid cell is retained only when it contains at least two valid samples. For inter-IPP-based variables, these samples are derived from distinct inter-IPP vectors whose midpoints fall within the same grid cell. This criterion reduces the influence of isolated observations and improves the robustness of the gridded products. In addition, the within-cell standard deviation of the contributing spatial-gradient samples is calculated as

$$\sigma\left(\nabla T_{\mathrm{V}}\right) = \sqrt{\left\langle\left(\nabla T_{\mathrm{V}}\right)^2\right\rangle - \left\langle\nabla T_{\mathrm{V}}\right\rangle^2} \tag{15}$$

where $\langle\cdot\rangle$ denotes the arithmetic mean over all valid samples within the grid cell. This quantity is released as GIX$_{\mathrm{std}}$ and provides a descriptive measure of the variability among gradient samples within each grid cell. Its value depends on the number and geometry of the contributing inter-IPP pairs, and some pairs may share common IPPs. Therefore, GIX$_{\mathrm{std}}$ is not interpreted as the statistical uncertainty of the grid-cell mean.

Table 4. Summary of Level-2 gridded variables released in the GIFT-BDS dataset.

Variable	Description	Grid spacing	Unit	Source quantity
VTEC	Vertical total electron content	$1° \times 1°$	TECU	T_V
$VTEC_t$	Time derivative of VTEC	$1° \times 1°$	$TECU\,min^{-1}$	$\frac{\partial T_V}{\partial t}$
ROTI	Rate of TEC index	$1° \times 1°$	$TECU\,min^{-1}$	I_{ROTI}
GIX	Magnitude of horizontal TEC spatial gradient	$0.25° \times 0.25°$	$10^{-3}\,TECU\,km^{-1}$	∇T_V
GIX_{std}	Standard deviation of GIX	$0.25° \times 0.25°$	$10^{-3}\,TECU\,km^{-1}$	$\sigma(\nabla T_V)$
GIX_x	Zonal component of horizontal TEC spatial gradient	$0.25° \times 0.25°$	$10^{-3}\,TECU\,km^{-1}$	$\frac{\partial T_V}{\partial x}$
GIX_y	Meridional component of horizontal TEC spatial gradient	$0.25° \times 0.25°$	$10^{-3}\,TECU\,km^{-1}$	$\frac{\partial T_V}{\partial y}$
$GIX_{t,x}$	Zonal component of the spatial gradient of the TEC temporal derivative	$0.25° \times 0.25°$	$10^{-3}\,TECU\,min^{-1}\,km^{-1}$	$\frac{\partial^2 T_V}{\partial x\,\partial t}$
$GIX_{t,y}$	Meridional component of the spatial gradient of the TEC temporal derivative	$0.25° \times 0.25°$	$10^{-3}\,TECU\,min^{-1}\,km^{-1}$	$\frac{\partial^2 T_V}{\partial y\,\partial t}$

3.3 Product quality assessment and uncertainty characterization

3.3.1 Level-1 STEC stability assessment

The Level-1 STEC records provide the primary input for the Level-2 VTEC and TEC-gradient products. Direct external validation of absolute STEC is difficult because STEC represents the electron content integrated along a specific receiver-satellite line of sight. Observations from other satellites sample different three-dimensional ionospheric paths, and similar IPP locations do not necessarily imply comparable absolute STEC values. Absolute STEC estimates are also affected by measurement noise, multipath, carrier-to-code leveling errors, and residual satellite and receiver DCB errors. The differential processing used for the Level-2 products largely reduces common bias components, although observation-dependent residuals may still propagate into the derived gradients. Differential STEC within continuous observation arcs has been widely used to assess relative TEC variations and consistency (Hernández-Pajares et al., 2017). Following this approach, each receiver-GEO link is evaluated using detrended STEC residuals. The resulting RMS characterizes the short-term stability and residual variability of Level-1 observations rather than their absolute accuracy. Figure 4 shows an example of the Level-1 GIFT-BDS GEO STEC product, the corresponding ROTI, and the absolute detrended STEC residual. The STEC record in Fig. 4a shows the temporal evolution of the LOS ionospheric delay after Level-1 processing. During the disturbed interval, enhanced residuals are accompanied by increased ROTI values. This correspondence shows that the detrended residual also responds to short-term ionospheric variability. During most of the day, the absolute detrended residual remains small, indicating stable short-term STEC behavior under relatively quiet conditions.

Figure 5 shows the daily median RMS of all valid LOS STEC residuals over the full data period, together with the corresponding interquartile range (IQR) and the daily number of valid IPPs. The RMS remains below 0.1 TECU for most of the record, with a mean value of about 0.06 TECU. Increased RMS values occur mainly during the equinox periods, when ionospheric irregularities are more frequent in the low-latitude region. The daily number of valid IPPs remains relatively stable, typically ranging between 800 and 950. These results indicate stable short-term Level-1 STEC behavior over most of the data period. The enhanced RMS during disturbed periods also confirms the sensitivity of this metric to short-term ionospheric variability. Station maintenance activities and data transmission interruptions may prevent valid GNSS observation files from being received at the data center. As a result, no processable observation files were available for 26 of the 531 d covered by the released dataset.

3.3.2 Internal consistency of Level-2 products

The internal consistency of the Level-2 gradient products depends on the stability of the GEO observation geometry. Although GEO satellites remain nearly stationary relative to the ground, small orbital variations introduce minor changes in IPP geometry and may affect the derived gradient estimates (Li et al., 2023).

Figure 6 presents an example of the Level-2 GIFT-BDS products at a representative epoch. The products include all variables listed in Table 4. The quantitative system-level consistency assessment is based on the relationship be-

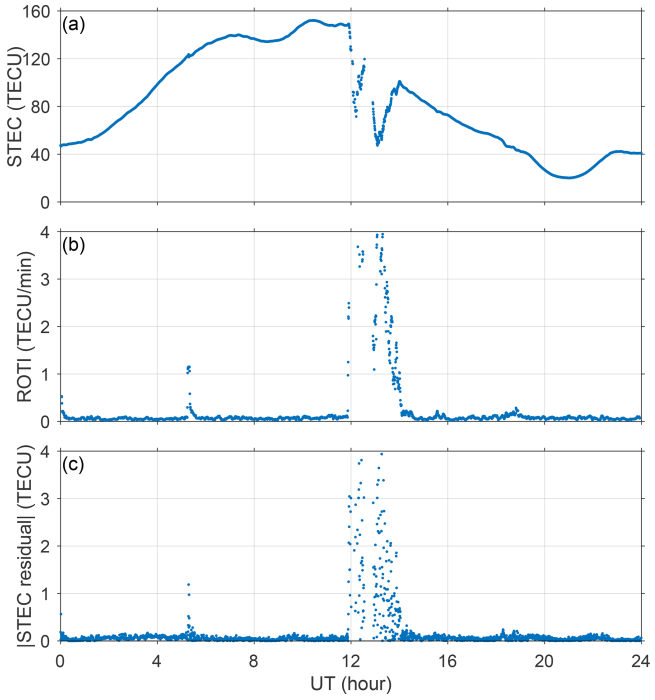


Figure 4. Example of the Level-1 GIFT-BDS GEO STEC products and the absolute residual of detrended STEC. The example corresponds to the BDS GEO satellite C01 on 21 September 2024. The IPP is located at 23.13° N and 120.92° E. **(a)** STEC record in the Level-1 product. **(b)** ROTI derived from the STEC. **(c)** Absolute residual of detrended STEC.

tween the temporal and spatial derivatives of the TEC field. Specifically, the spatial variation of the local VTEC temporal change $(\partial(\partial T_V/\partial t)/\partial S)$ should be compatible with the temporal variation of the horizontal VTEC gradient $(\partial(\partial T_V/\partial S)/\partial t)$ under an internally consistent gridded TEC field. This relationship is expected to hold more clearly when residual errors are low and the GEO observation geometry is temporally stable. In this case, the spatial variation of the TEC temporal change and the temporal variation of the TEC spatial gradient provide two complementary descriptions of the same evolving TEC distribution.

Direct external validation of the Level-2 gradient products is limited by the lack of independent two-dimensional TEC-gradient observations with comparable spatial and temporal resolution over China. Following Li et al. (2025b), the asymmetry of mixed spatiotemporal partial derivatives is used to assess the internal consistency of the derived gradients. This metric evaluates the agreement between two independent derivative paths without requiring an external gradient reference. The asymmetry metric is defined as:

$$\text{Asymmetry} = \sqrt{\left(\frac{\partial^2 T_V}{\partial t\,\partial x} - \frac{\partial^2 T_V}{\partial x\,\partial t}\right)^2 + \left(\frac{\partial^2 T_V}{\partial t\,\partial y} - \frac{\partial^2 T_V}{\partial y\,\partial t}\right)^2} \quad (16)$$

where the terms represent the differences between the two orders of mixed partial derivatives in the zonal and meridional directions, respectively. For an ideal, smooth TEC distribution on the ionospheric shell, the asymmetry should approach zero. In practice, non-zero values may result from residual measurement noise, small geometry variations, mapping effects, gridding effects, and genuine ionospheric variability. Therefore, the asymmetry metric characterizes system-level internal consistency rather than absolute gradient error.

Figure 7 summarizes the daily internal consistency statistics of the Level-2 gradient products. The daily median mixed-partial-derivative asymmetry remains close to 0.06×10^{-3} TECU min^{-1} km^{-1} for most of the record, with no significant long-term trend. The interquartile range is also generally stable throughout the period, indicating that the combined effects of geometry-related variability, residual observation errors, and gridding noise on the Level-2 gradient products are limited and temporally consistent. The long-term behavior of this metric supports the internal-consistency assessment of the GIFT-BDS Level-2 gridded gradient products.

3.4 Comparison with GIM-derived gradient estimates

A comparison with GIM-derived gradients is used to examine the spatial structures represented by the GIFT-BDS Level-2 products. The CAS GIM provides a global ionospheric representation at a relatively coarse spatial resolution. Its coarse spatial sampling and associated smoothing attenuate localized gradient amplitudes, making it unsuitable as a quantitative reference for the accuracy of the high-resolution GIFT-BDS gradients. The comparison is thus restricted to large-scale spatial structures and differences in spatial resolution.

Figure 8 compares the temporal evolution of VTEC and spatial gradient quantities along the 115° E meridian between 20° N and 30° N during 5–7 April 2025. Panels (a), (c), (e), (g) show CAS GIM-derived results, while panels (b), (d), (f), (h) show the corresponding GIFT-BDS products. The CAS GIM has a spatial resolution of 2.5° in latitude and 5° in longitude, whereas the GIFT-BDS TEC-gradient products are provided on a $0.25° \times 0.25°$ grid. Both products reproduce the broad diurnal evolution of VTEC over the selected latitude range, including the daytime enhancement and nighttime decay. However, the GIM-derived results are smoother in space and time, as expected from the coarser grid spacing. Their corresponding gradient structures are weaker and broader, with limited representation of localized gradient features. In contrast, the GIFT-BDS products show sharper and more localized gradient enhancements in GIX, together with meridional and zonal gradient structures in GIX_y and GIX_x. The difference is especially evident near the low-latitude crest region, where GIFT-BDS captures narrow and rapidly evolving meridional gradient features that are largely smoothed in the GIM-derived results.

The comparison illustrates the additional regional detail provided by the GIFT-BDS Level-2 gradient products. The

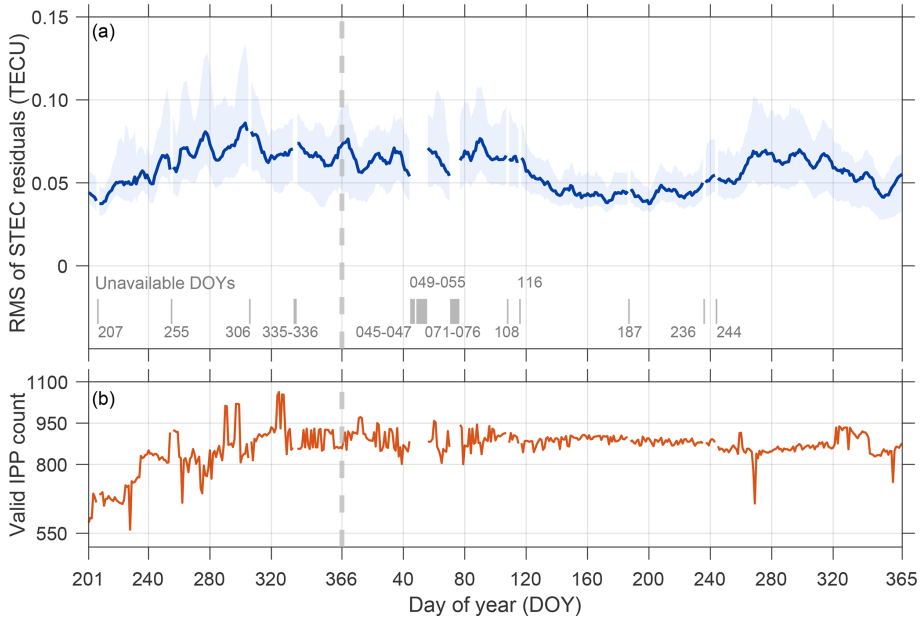


Figure 5. Daily Level-1 STEC stability statistics for the GIFT-BDS dataset over the full period. **(a)** Daily RMS statistics of detrended line-of-sight STEC residuals. The blue curve denotes the 7 d moving mean of the daily median RMS, and the light-blue shading represents the interquartile range (IQR; 25th–75th percentiles) of the daily RMS values. Gray vertical bars and labels indicate DOYs for which no processable observation files were available. **(b)** Daily number of valid IPPs used in the Level-1 product generation. The vertical dashed line marks the boundary between 2024 and 2025.

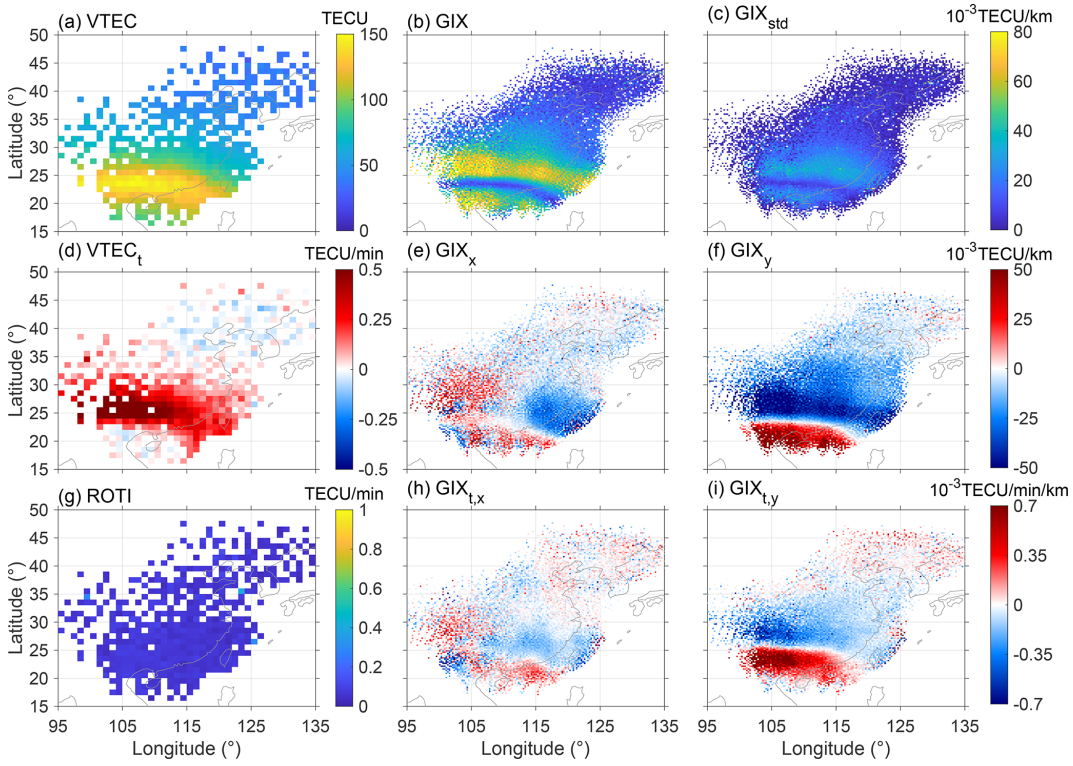


Figure 6. Example GIFT-BDS TEC gradient products at 13:40 LT (115° E) on 21 September 2024. All panels display grid-mean values. Panels **(b)**, **(c)**, **(e)**, **(f)**, **(h)**, and **(i)** use a 0.25° × 0.25° grid, while panels **(a)**, **(d)** and **(g)** use a 1° × 1° grid. The positive x and y directions denote eastward and northward, respectively.

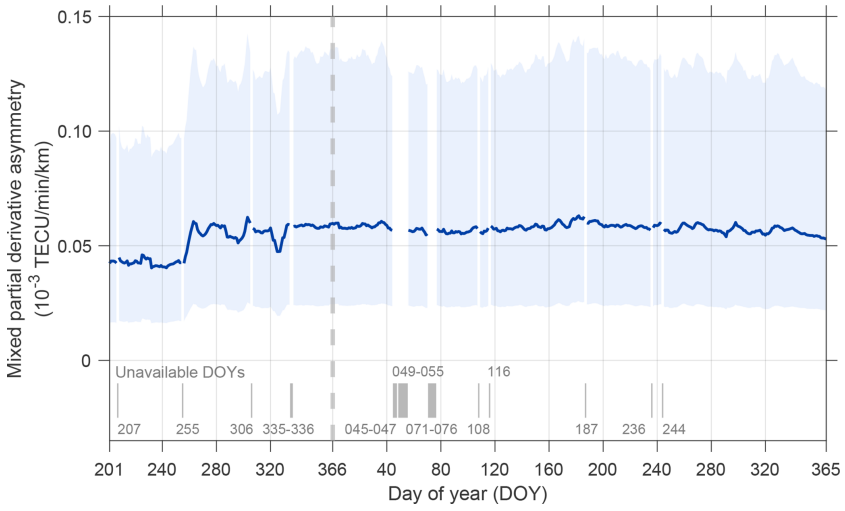


Figure 7. Daily internal-consistency statistics of the GIFT-BDS Level-2 gradient products over the full data period. The blue curve shows the 7 d moving mean of the daily median mixed-partial-derivative asymmetry, and the blue shading denotes the interquartile range (IQR; P25–P75). Gray bars and labels mark DOYs without valid observations. The vertical dashed line indicates the boundary between 2024 and 2025.

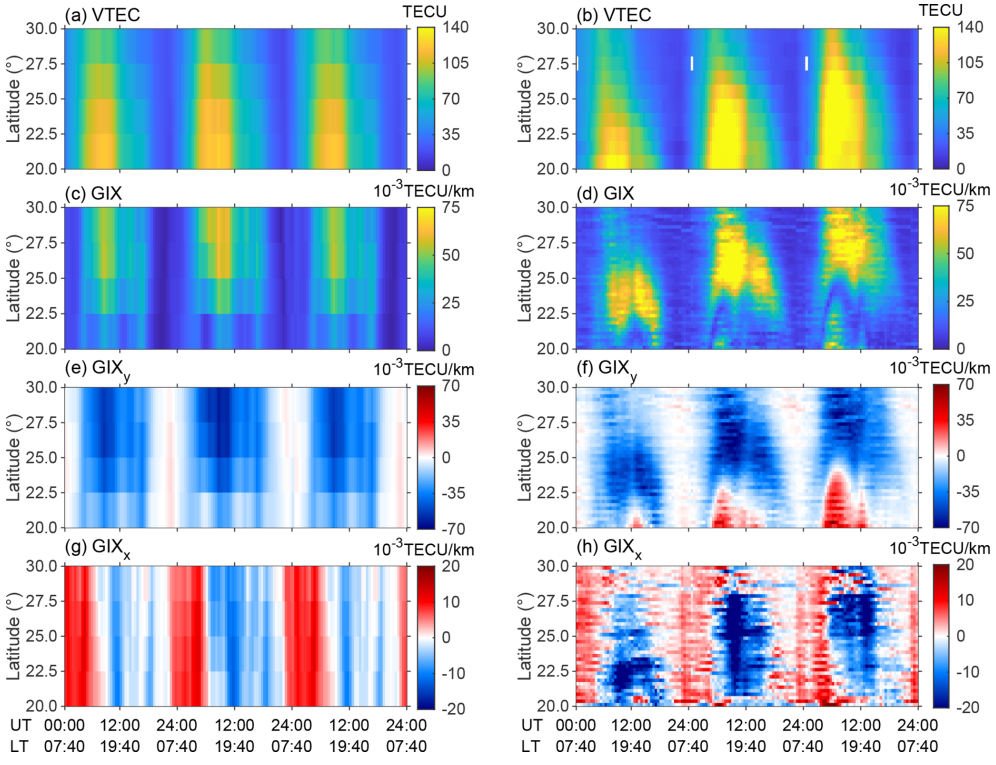


Figure 8. Latitude-time variations of ionospheric TEC and its spatial gradients along the 115° E meridian from 5–7 April 2025. The left panels are derived from the CAS GIM, and the right panels are derived from the GIFT-BDS dataset. Panels **(a)**, **(b)** show VTEC, **(c)**, **(d)** show GIX, **(e)**, **(f)** show GIX$_y$, and **(g)**, **(h)** show GIX$_x$ over 20–30° N. Time is labeled in UT, with the corresponding local time at 115° E shown below. Positive GIX$_x$ and GIX$_y$ denote eastward and northward TEC gradient components, respectively. The CAS GIM has a nominal grid spacing of 5° × 2.5°, whereas the GIFT-BDS TEC-gradient products are provided on a 0.25° × 0.25° grid.

GEO-derived products resolve localized TEC-gradient structures and their short-term evolutions at finer spatial scales, whereas the GIM-derived gradients provide the large-scale ionospheric background for comparison.

4 Example applications

This section provides two examples to illustrate possible uses of the released products. The first example uses GIX and its directional components to describe event-scale and seasonal TEC gradient structures associated with daytime Equatorial Ionization Anomaly (EIA) development and nighttime Equatorial Plasma Bubble (EPB) activity. The second example compares GIFT-BDS-based GIX indicators with PPP and network RTK (NRTK) positioning performance during disturbed ionospheric conditions.

4.1 Example use for event-scale and seasonal TEC-gradient characterization

EIA development and EPB activity are representative low-latitude ionospheric processes over China and its surrounding regions. EIA occurs during daytime and is characterized by a trough in electron density near the magnetic equator and two anomaly crests at low magnetic latitudes. It is formed by the fountain effect, which lifts plasma upward and redistributes it along geomagnetic field lines (Chen et al., 2023; Nigussie et al., 2022). EPBs mainly occur at night and appear as depleted plasma density structures that originate in the equatorial ionosphere and may extend to low latitudes. They are often aligned nearly north–south and drift zonally, producing pronounced spatial gradients and irregular perturbations (Li et al., 2021a; Song et al., 2025). Because both phenomena exhibit clear spatial patterns and temporal evolution, they provide suitable examples for illustrating the use of GIFT-BDS in describing regional TEC gradient structures.

Figure 9 shows GIX and its directional components for a daytime EIA-related structure and a nighttime EPB-related structure on 21 September 2024, together with their evolution along selected meridional and zonal sections. In panel (a), enhanced GIX values appear on both flanks of the daytime EIA crest at low latitudes, indicating enhanced horizontal TEC gradients associated with the anomaly structure. Panel (b) shows the corresponding meridional TEC gradient pattern. The near-zero transition zone marks the approximate crest location, while the opposite signs on the two sides indicate rapid TEC decay away from the crest. In panel (c), nighttime EPB-related structures appear as narrow, nearly meridional bands of enhanced GIX. Panel (d) shows the associated zonal TEC gradient component, with enhanced GIX_x values along the edges of the depletion structures. Along 115° E, panel (e) shows the daytime enhancement of GIX around the EIA crest region, while panel (f) illustrates the associated meridional gradient pattern through the sign reversal of GIX_y and the displacement of the near-zero transition zone. Along 23.5° N, panel (g) shows the zonal evolution of EPB-related GIX_x enhancements in longitude-time space. These examples illustrate how GIFT-BDS can be used to follow regional TEC-gradient structures under daytime and nighttime ionospheric conditions.

Figure 10 extends the event-scale example to a longer timescale and illustrates the seasonal variability of daytime EIA-related gradient structures. To emphasize the latitudinal organization of the anomaly, GIX and GIX_y are first averaged over 100–120° E and then averaged within a fixed local time window of 13:40–17:40 LT for each day. This averaging reduces short-term longitudinal variability and provides a consistent daytime view of day-to-day and seasonal changes. In panel (a), enhanced GIX values are mainly around the EIA crest region. The intensity and latitudinal extent of these gradients show clear seasonal modulation, with stronger and broader structures during the equinox seasons and weaker signatures around the June solstice. Panel (b) shows the corresponding latitude-DOY distribution of GIX_y, which represents the meridional TEC gradient pattern. Positive values south of the crest region and negative values to the north indicate opposite meridional TEC gradient directions on the two sides of the EIA crest. The near-zero transition region marks the approximate crest location. Together with the event-scale example in Fig. 9, these results illustrate the use of GIFT-BDS for describing TEC-gradient morphology from event to seasonal timescales.

4.2 Example use for GNSS positioning-related analysis

GNSS positioning performance can be notably affected by ionospheric disturbances, particularly under conditions of rapid spatial and temporal variations in electron density. Such effects are typically more pronounced during disturbed ionospheric periods, when ionospheric irregularities such as EPBs and sharp TEC gradients occur more frequently. GIX quantifies the magnitude of horizontal TEC spatial gradients and serves as an indicator of the regional TEC gradient environment. Previous studies have reported associations between enhanced GIX and degraded PPP performance during geomagnetic storms (Fu et al., 2025b; Nykiel et al., 2024). In this section, GIFT-BDS is used to illustrate the association between regional TEC gradient activity and PPP/NRTK positioning performance.

Figure 11 shows the temporal evolution of TEC gradient activity and PPP/NRTK positioning performance over 15–25° N and 100–120° E during a geomagnetically disturbed period. The ionospheric conditions are characterized using two GIFT-BDS variables: GIX, which quantifies horizontal TEC spatial gradient intensity, and ROTI, which describes short-term TEC temporal variability. In this case, enhanced GIX and ROTI structures are observed during the disturbed interval, with an apparent eastward evolution in panels (d) and (e). Panels (a) and (b) show the horizontal and vertical RMS of PPP positioning errors for 48 stations in the selected

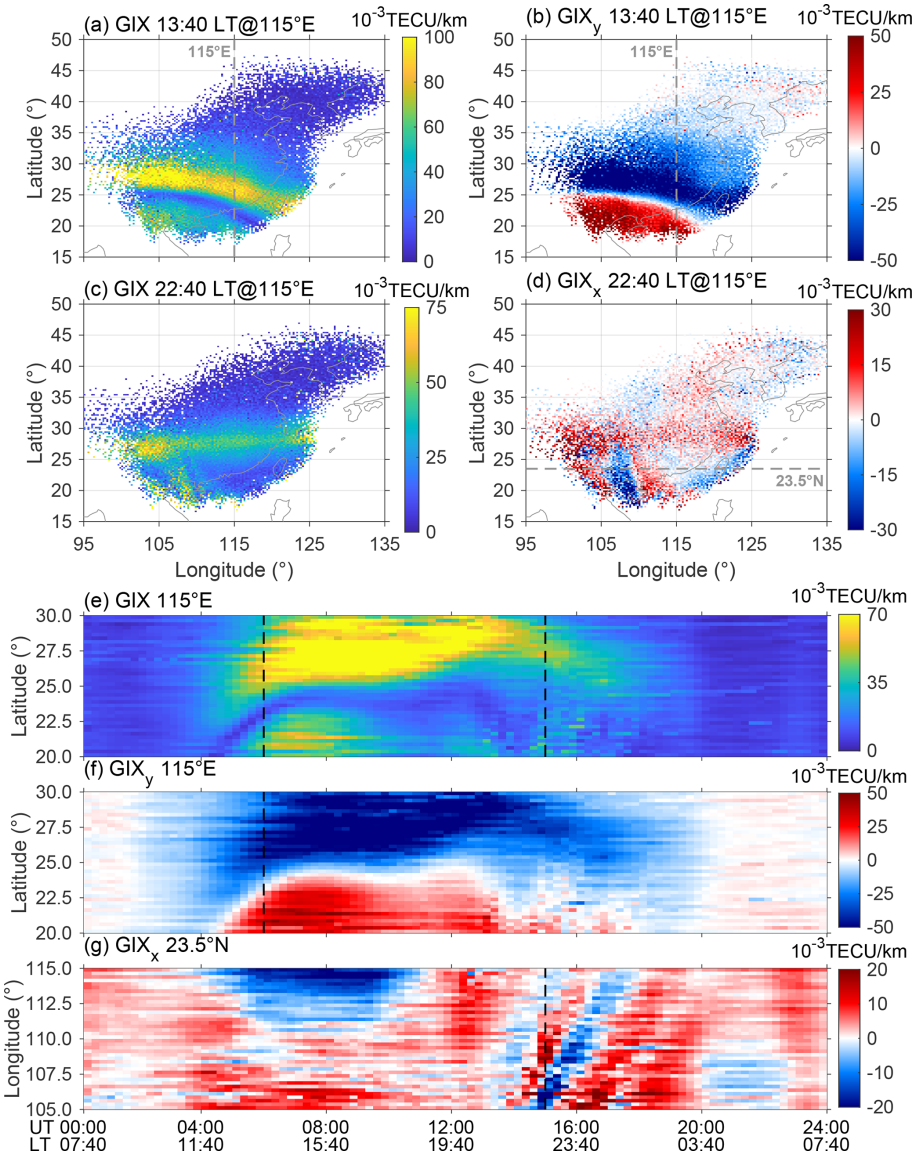


Figure 9. Example GIFT-BDS TEC gradient products on 21 September 2024. Panels **(a)**, **(b)** show GIX and its meridional component GIX$_y$ at 13:40 LT, and **(c)**, **(d)** show GIX and its zonal component GIX$_x$ at 22:40 LT over the region 15–50° N, 95–135° E. The dashed line in **(a)**, **(b)** marks the 115° E meridian used for the latitude-time sections in **(e)**, **(f)**, and the dashed line in **(d)** marks the 23.5° N parallel used for the longitude-time section in **(g)**. Panels **(e)**, **(f)** present latitude-time variations of GIX and GIX$_y$ along 115° E over 20–30° N, and **(g)** presents a longitude-time variation of GIX$_x$ along 23.5° N over 105–115° E. The vertical dashed lines in **(e)**–**(g)** indicate 13:40 and 22:40 LT, corresponding to the snapshots in **(a)**, **(b)** and **(c)**, **(d)**, respectively.

region. In both panels, the station-mean and P95 RMS values increase during the interval of enhanced TEC gradient activity. Panel (c) compares the mean horizontal error of NRTK solutions in Hong Kong with the collocated GIX time series at 23° N, 113° E. The enhanced and rapidly varying GIX values are consistent with the passage of EPB-related gradient structures over the region. Increased NRTK errors occur during intervals of enhanced GIX, showing a temporal association between regional TEC gradient activity and positioning degradation. This event-level comparison illustrates the correspondence between regional TEC gradient activity and GNSS positioning performance.

Figure 12 presents a statistical analysis of NRTK horizontal positioning errors and collocated GIX values over the Hong Kong network. Note that TEC-gradient structures over low-latitude China are produced by different ionospheric processes, and enhanced GIX values may occur during both daytime EIA development and nighttime EPB activity. Since daytime EIA conditions are generally associated with smoother electron density variations and lower ROTI,

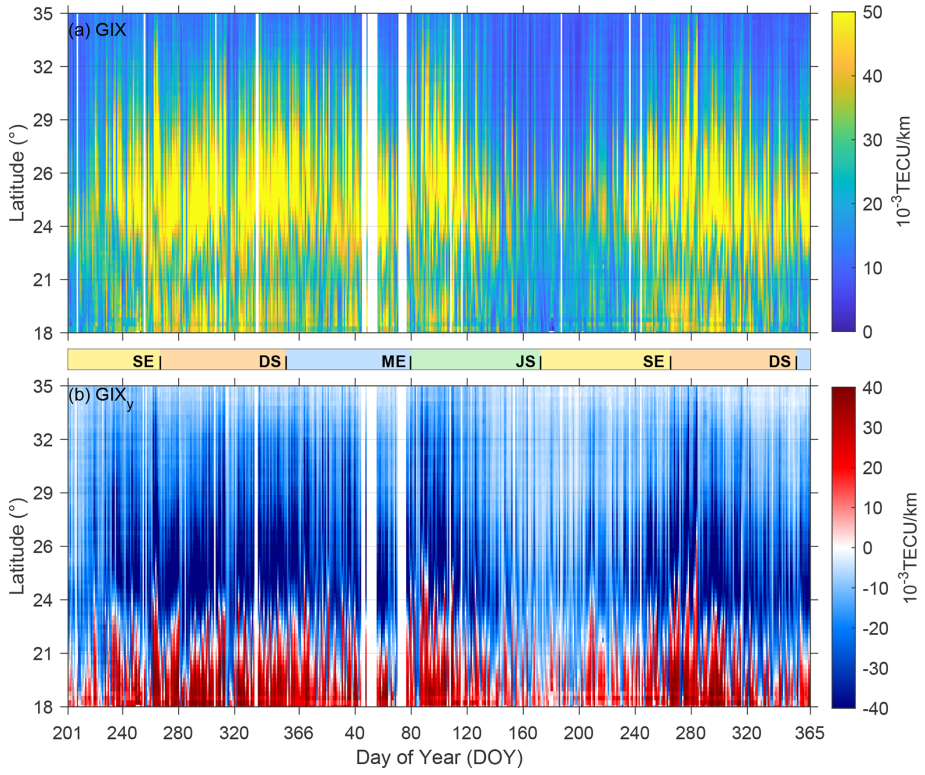


Figure 10. Seasonal variability of daytime GIFT-BDS TEC gradient products from mid-2024 to the end of 2025. Panels **(a)** and **(b)** show latitude-DOY variations of longitude-averaged GIX and its meridional component GIX_y, respectively, over 18–35° N and 100–120° E. For each day, the values are first averaged over 100–120° E and then averaged within the local-time window of 13:40–17:40 LT referenced to 115° E. White gaps indicate days or latitude bins without valid gridded products. The colored bar below **(a)** indicates the seasonal partition used in the analysis: SE, September equinox; DS, December solstice; ME, March equinox; JS, June solstice.

this analysis is restricted to nighttime conditions during the September-equinox interval, when enhanced GIX values are more likely associated with EPB-related structures. Panel (a) shows the relationship between the median NRTK horizontal positioning error and GIX. Large-error samples in the 2–15 m range tend to occur at higher GIX values, with a correlation coefficient of 0.752 for this subset. In contrast, smaller-error samples below 2 m show weaker dependence on GIX, indicating that other error sources may contribute substantially under moderate-error conditions. Panel (b) shows the occurrence probabilities of the two error ranges as a function of GIX. The probability of large NRTK errors increases with GIX, whereas the moderate-error range does not show the same monotonic behavior. These results further show a statistical association between enhanced regional TEC gradients and degraded NRTK positioning performance. Additionally, regional GIX information could support positioning quality control by identifying periods or areas with enhanced TEC gradient activity. It could also provide auxiliary information for observation weighting. Further evaluation is needed to determine how these applications depend on positioning strategies, satellite geometry, and ionospheric delay treatment.

5 Data availability

The GIFT-BDS dataset used in this paper covers the period from 19 July 2024 to 31 December 2025, corresponding to DOY 201 of 2024 to DOY 365 of 2025. The versioned public release is available at https://doi.org/10.5281/zenodo.21090695 (Li et al., 2026a). The release contains Level-1 GEO-derived STEC records, Level-2 gridded TEC and TEC-gradient products, quality-control descriptors, and associated metadata. Operational GIFT-BDS products are available at https://data.bdsmart.cn/pub/campaign/iono/ (last access: 23 November 2026). They are generated using the same processing strategy as the versioned release and are updated regularly with a processing latency of several days. These operational products should be regarded as provisional updates until they are included in a subsequent versioned release.

6 Conclusion

This paper presents GIFT-BDS, a regularly updated regional ionospheric TEC and GIX dataset over China. The dataset is generated from a fixed-geometry observation network com-

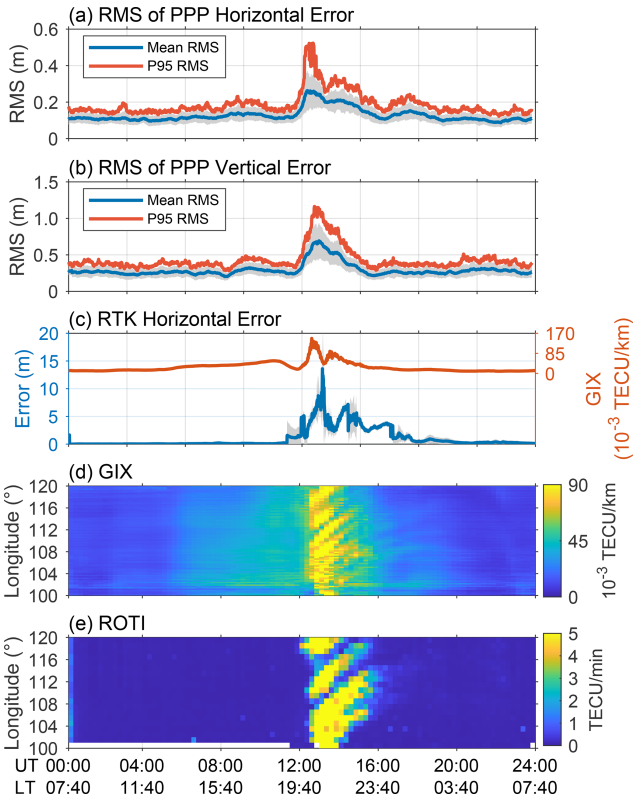


Figure 11. Example use of GIFT-BDS for comparing TEC gradient activity with GNSS positioning performance during the 7 October 2024 geomagnetic storm. Panels **(a)** and **(b)** show the horizontal and vertical RMS of PPP positioning errors, respectively, computed from 48 stations within 15–25° N and 100–120° E. The blue curves denote the station-mean RMS, the orange curves denote the 95th percentile (P95) of station-wise RMS, and gray shaded envelopes indicate ±1 standard deviation about the mean. Panel **(c)** shows the mean horizontal error of network RTK solutions from 12 stations in Hong Kong, with an average baseline length of about 20 km, together with the collocated GIX time series at 23° N, 113° E. The gray envelope indicates ±1 standard deviation across the NRTK stations. Panels **(d)** and **(e)** show the latitude-averaged GIX and ROTI, respectively, over 15–25° N and 100–120° E. The time axis is labeled in UT, with the corresponding LT at 115° E shown below.

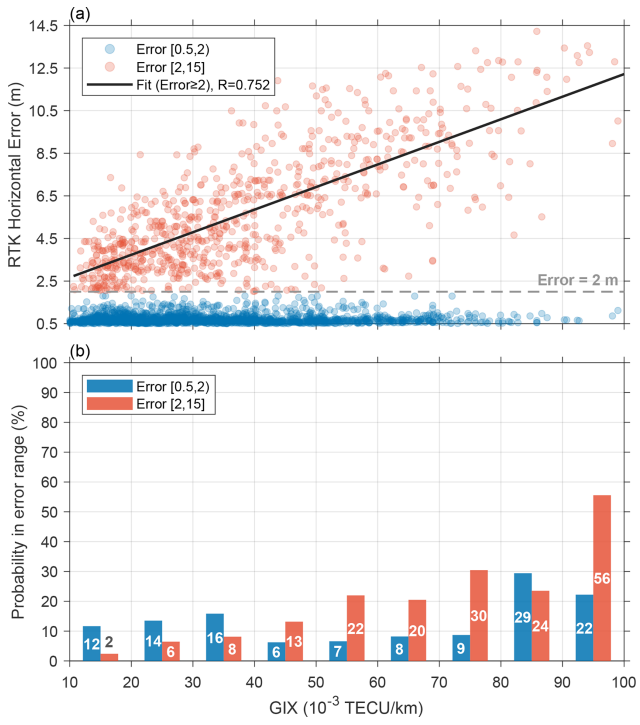


Figure 12. Example use of GIFT-BDS for relating collocated GIX to NRTK horizontal positioning errors in Hong Kong (23° N, 113° E) from 10 August–29 October 2024. The analysis uses a 12-station network RTK configuration with a mean baseline length of about 20 km. GNSS solutions are computed at 30 s intervals and summarized at a 15 min sampling cadence. For each 15 min interval, the median horizontal positioning error across the NRTK stations is compared with the collocated GIX value. Panel **(a)** shows the epoch-wise median horizontal error as a function of GIX, separated into two error ranges, 0.5–2 m (blue) and 2–15 m (orange). The solid black line shows a regression fit to the 2–15 m samples, and the dashed gray line marks the 2 m threshold used here to indicate severe positioning degradation. Panel **(b)** shows the occurrence probability of the two error ranges as a function of GIX, obtained by binning the GIX values. Numbers within the bars denote the corresponding percentages.

bining more than 200 ground-based GNSS receivers and five BeiDou GEO satellites. The near-stationary receiver-satellite geometry provides repeated sampling of nearly fixed ionospheric pierce points and supports the estimation of regional TEC-gradient quantities. The released products are organized into two levels. Level-1 provides GEO-derived STEC time series for individual receiver-satellite links, while Level-2 provides gridded TEC, ROTI and GIX products. The TEC gradient products are provided on a $0.25° \times 0.25°$ grid with a temporal resolution of 15 min.

The quality and consistency assessments support the reliability and usability of the released dataset. The Level-1 STEC records show short-term stability at the sub-TECU level, as assessed from detrended STEC residuals. The Level-2 gradient products show temporally stable internal consistency under the BeiDou GEO observation geometry, based on the mixed-partial-derivative asymmetry diagnostic. Comparison with GIM-derived gradients further illustrates the added regional detail and temporal continuity provided by GIFT-BDS. The example applications show how the dataset can be used to describe EIA-related gradient morphology, EPB-related gradient structures, seasonal TEC gradient variability, and ionospheric conditions relevant to PPP and NRTK performance analyses.

GIFT-BDS provides a new regional data resource for ionospheric process studies, space-weather monitoring, and GNSS application analyses over China. The archived release used in this paper is complemented by regularly updated op-

erational products. Future versions will extend the temporal coverage, improve product completeness, and further refine the quality-control procedures and metadata information to support long-term use of the dataset.

Author contributions. NW and JZ contributed to the conceptualization; ZL, JZ, NW, YH, YY, XW and AL were involved in the methodology; ZL and NW assisted in the formal analysis and investigation; ZL and JZ contributed to writing – original draft preparation; ZL, JZ, NW, YH, XW, NJ, and MH helped in writing – review and editing; JZ, NW, YH and XW acquired the funding; NW, JZ, ZsL, YH and XW contributed to the resources; JZ, NW, YH, AL, XW and ZsL contributed to the supervision. All authors have read and agreed to the final version of the manuscript.

Competing interests. The contact author has declared that none of the authors has any competing interests.

Disclaimer. Publisher's note: Copernicus Publications remains neutral with regard to jurisdictional claims made in the text, published maps, institutional affiliations, or any other geographical representation in this paper. The authors bear the ultimate responsibility for providing appropriate place names. Views expressed in the text are those of the authors and do not necessarily reflect the views of the publisher.

Acknowledgements. We are grateful to the Chinese Academy of Sciences (CAS, https://data.bdsmart.cn/pub/, last access: 23 November 2026) and the International GNSS Service (IGS) for providing GNSS data. The authors also acknowledge the technical support from Chenxu Wang, Kai Wei, and Qingbo Meng, members of the BDSmart research group at Qilu Aerospace Information Research Institute.

Financial support. This work was supported by the National Natural Science Foundation of China (grant nos. 42374181, 42374186, and 42441814), Shandong Key R&D Program (grant no. 2024CXGC00116) and Jinan Haiyou Leading Talents Of Industry, Key Innovation Team of China Meteorological Administration "Space Weather Monitoring and Alerting" (grant no. CMA2024ZD01), "Ionospheric Forecast and Alerting" Youth Innovation Team (grant no. CMA2024QN09).

Review statement. This paper was edited by Guanyu Huang and reviewed by two anonymous referees.

References

Abdu, M. A.: Outstanding problems in the equatorial ionosphere–thermosphere electrodynamics relevant to spread F, J. Atmos. Sol.-Terr. Phy., 63, 869–884, https://doi.org/10.1016/S1364-6826(00)00201-7, 2001.

Astafyeva, E.: Ionospheric Detection of Natural Hazards, Rev. Geophys., 57, 1265–1288, https://doi.org/10.1029/2019RG000668, 2019.

Astafyeva, E., Zakharenkova, I., and Förster, M.: Ionospheric response to the 2015 St. Patrick's Day storm: A global multi-instrumental overview, J. Geophys. Res.-Space, 120, 9023–9037, https://doi.org/10.1002/2015JA021629, 2015.

Balan, N., Liu, L., and Le, H.: A brief review of equatorial ionization anomaly and ionospheric irregularities, Earth Planet. Phys., 2, 257–275, https://doi.org/10.26464/epp2018025, 2018.

Buonsanto, M. J.: Ionospheric Storms – A Review, Space Sci. Rev., 88, 563–601, https://doi.org/10.1023/A:1005107532631, 1999.

Chen, J., Zhong, J., Hao, Y., Wan, X., Li, Q., Tang, Z., Song, X., Han, H., Wang, K., Kuai, J., and Ren, A.: Horizontal Spatial Correlation of the Ionospheric Day-To-Day Variations at Low Latitudes Based on GOLD Nmax Data, Space Weather, 21, e2023SW003627, https://doi.org/10.1029/2023SW003627, 2023.

Chen, P., Yao, Y., and Yao, W.: Global ionosphere maps based on GNSS, satellite altimetry, radio occultation and DORIS, GPS Solut., 21, 639–650, https://doi.org/10.1007/s10291-016-0554-9, 2017.

Chen, Y., Liu, L., Le, H., Wan, W., and Zhang, H.: Equatorial ionization anomaly in the low-latitude topside ionosphere: Local time evolution and longitudinal difference, J. Geophys. Res.-Space, 121, 7166–7182, https://doi.org/10.1002/2016JA022394, 2016.

Chen, Y., Aa, E., Yuan, T., Zhang, S., Shen, H., Yue, X., Xu, H., Liu, S., Wang, X., Huang, W., Li, H., Luo, B., Zhang, Q., and Wang, C.: The extreme depletion of ionospheric electron density and its hemispheric asymmetry during the May 2024 storm, Natl. Sci. Rev., 12, nwaf307, https://doi.org/10.1093/nsr/nwaf307, 2025.

Francis, S. H.: A theory of medium-scale traveling ionospheric disturbances, J. Geophys. Res., 79, 5245–5260, https://doi.org/10.1029/JA079i034p05245, 1974.

Fu, Z., Shen, X., Liu, Q., and Wang, N.: Ionospheric Disturbances from the 2022 Hunga-Tonga Volcanic Eruption: Impacts on TEC Spatial Gradients and GNSS Positioning Accuracy Across the Japan Region, Remote Sens.-Basel, 17, 3108, https://doi.org/10.3390/rs17173108, 2025a.

Fu, Z., Wang, N., Shen, X., and Li, A.: Temporal and Spatial Analysis of the Impact of the 2015 St. Patrick's Day Geomagnetic Storm on Ionospheric TEC Gradients and GNSS Positioning in China Using GIX and ROTI Indices, Remote Sens.-Basel, 17, 2027, https://doi.org/10.3390/rs17122027, 2025b.

Hedin, A. E.: MSIS-86 Thermospheric Model, J. Geophys. Res., 92, 4649–4662, https://doi.org/10.1029/JA092iA05p04649, 1987.

Hernández-Pajares, M., Juan, J. M., Sanz, J., Orus, R., Garcia-Rigo, A., Feltens, J., Komjathy, A., Schaer, S. C., and Krankowski, A.: The IGS VTEC maps: a reliable source of ionospheric information since 1998, J. Geodesy, 83, 263–275, https://doi.org/10.1007/s00190-008-0266-1, 2009.

Hernández-Pajares, M., Roma-Dollase, D., Krankowski, A., García-Rigo, A., and Orús-Pérez, R.: Methodology and consistency of slant and vertical assessments for ionospheric electron content models, J. Geodesy, 91, 1405–1414, https://doi.org/10.1007/s00190-017-1032-z, 2017.

Hu, J., Ruan, H., Huang, F., Gu, S., and Dou, X.: Assessment of International GNSS Service Global Ionosphere Map products over China region based on measurements from the Crustal Movement Observation Network of China, Earth Planet. Phys., 8, 400–407, https://doi.org/10.26464/epp2024004, 2024.

Huang, F., Lei, J., Yue, X., Li, Z., Zhang, N., Cai, Y., Zhang, S., Wang, Y., Zhong, J., and Luan, X.: Interplay of Gravity Waves and Disturbance Electric Fields to the Abnormal Ionospheric Variations During the 11 May 2024 Superstorm, AGU Adv., 6, e2024AV001379, https://doi.org/10.1029/2024AV001379, 2025.

Jakowski, N. and Hoque, M. M.: Estimation of Spatial Gradients and Temporal Variations of the Total Electron Content Using Ground-Based GNSS Measurements, Space Weather, 17, 339–356, https://doi.org/10.1029/2018SW002119, 2019.

Jakowski, N., Hoque, M. M., Cahuasquí, J. A., and Nykiel, G.: Characterizing ionospheric perturbations with refined gradient ionosphere indices, GPS Solut., 30, 177, https://doi.org/10.1007/s10291-026-02143-4, 2026.

Kenyeres, A. and Bruyninx, C.: EPN coordinate time series monitoring for reference frame maintenance, GPS Solut., 8, 200–209, https://doi.org/10.1007/s10291-004-0104-8, 2004.

Kim, M., Seo, J., and Lee, J.: A Comprehensive Method for GNSS Data Quality Determination to Improve Ionospheric Data Analysis, Sensors-Basel, 14, 14971–14993, https://doi.org/10.3390/s140814971, 2014.

Klobuchar, J.: Ionospheric Time-Delay Algorithm for Single-Frequency GPS Users, IEEE T. Aerosp. Electron. Syst., AES-23, 325–331, https://doi.org/10.1109/taes.1987.310829, 1987.

Li, G., Ning, B., Otsuka, Y., Abdu, M. A., Abadi, P., Liu, Z., Spogli, L., and Wan, W.: Challenges to Equatorial Plasma Bubble and Ionospheric Scintillation Short-Term Forecasting and Future Aspects in East and Southeast Asia, Surv. Geophys., 42, 201–238, https://doi.org/10.1007/s10712-020-09613-5, 2021a.

Li, M., Yuan, Y., Wang, N., Liu, T., and Chen, Y.: Estimation and analysis of the short-term variations of multi-GNSS receiver differential code biases using global ionosphere maps, J. Geodesy, 92, 889–903, https://doi.org/10.1007/s00190-017-1101-3, 2018.

Li, R., Lei, J., Huang, F., Liu, F., Zhang, S., Chen, X., Luan, X., Yang, Z., Dang, T., and Dou, X.: Ionospheric Lamb Waves With Conical Phase Fronts Following the 2022 Tonga Eruption Unveiled by BeiDou GEO Observations, Geophys. Res. Lett., 52, e2025GL114976, https://doi.org/10.1029/2025GL114976, 2025a.

Li, Z., Wang, N., Liu, A., Yuan, Y., Wang, L., Hernández-Pajares, M., Krankowski, A., and Yuan, H.: Status of CAS global ionospheric maps after the maximum of solar cycle 24, Satell. Navig., 2, 19, https://doi.org/10.1186/s43020-021-00050-2, 2021b.

Li, Z., Zhong, J., Hao, Y., Zhang, M., Niu, J., Wan, X., Huang, F., Han, H., Song, X., and Chen, J.: Assessment of the orbital variations of GNSS GEO and IGSO satellites for monitoring ionospheric TEC, GPS Solut., 27, 62, https://doi.org/10.1007/s10291-023-01403-x, 2023.

Li, Z., Zhong, J., Wang, N., Hao, Y., Wan, X., Jakowski, N., Hoque, M. M., Liu, A., Li, Z., Liu, R., and Nykiel, G.: Ionospheric gradient estimation using ground-based GEO observations for monitoring multi-scale ionospheric dynamics, Satell. Navig., 6, 30, https://doi.org/10.1186/s43020-025-00187-4, 2025b.

Li, Z., Wang, N., and Zhong, J.: GIFT-BDS: A high-resolution TEC and Gradient Ionospheric Index dataset over China derived from BeiDou GEO fixed-geometry observations, Zenodo [data set], https://doi.org/10.5281/zenodo.21090695, 2026a.

Li, Z., Zhong, J., Wang, N., Hao, Y., Wan, X., and Zhao, J.: Performance of GNSS dual-frequency combinations in estimating TEC based on ROTI, GPS Solut., 30, 25, https://doi.org/10.1007/s10291-025-01987-6, 2026b.

Liu, B., Liu, L., Liu, A., Yang, Y., Zhao, X., Li, Z., Yue, X., Liu, J., Le, H., Chen, Y., Zhang, R., and Li, W.: Study of regional ionospheric structures and their impacts on SPP and PPP with multi-instrument observations in the Asian sector, Satell. Navig., 7, 5, https://doi.org/10.1186/s43020-026-00191-2, 2026.

Liu, Q., Hernández-Pajares, M., Yang, H., Monte-Moreno, E., Roma-Dollase, D., García-Rigo, A., Li, Z., Wang, N., Laurichesse, D., Blot, A., Zhao, Q., Zhang, Q., Hauschild, A., Agrotis, L., Schmitz, M., Wübbena, G., Stürze, A., Krankowski, A., Schaer, S., Feltens, J., Komjathy, A., and Ghoddousi-Fard, R.: The cooperative IGS RT-GIMs: a reliable estimation of the global ionospheric electron content distribution in real time, Earth Syst. Sci. Data, 13, 4567–4582, https://doi.org/10.5194/essd-13-4567-2021, 2021.

Ma, G., Fan, J., Wan, Q., and Li, J.: Error Characteristics of GNSS Derived TEC, Atmosphere-Basel, 13, 237, https://doi.org/10.3390/atmos13020237, 2022.

Mannucci, A. J., Wilson, B. D., Yuan, D. N., Ho, C. H., Lindqwister, U. J., and Runge, T. F.: A global mapping technique for GPS-derived ionospheric total electron content measurements, Radio Sci., 33, 565–582, https://doi.org/10.1029/97RS02707, 1998.

Montenbruck, O., Hauschild, A., and Steigenberger, P.: Differential Code Bias Estimation using Multi-GNSS Observations and Global Ionosphere Maps, Navigation, 61, 191–201, https://doi.org/10.1002/navi.64, 2014.

Nigussie, M., Jakowski, N., and Hoque, M.: Characterization and Climatological Modeling of Equatorial Ionization Anomaly (EIA) Crest Position, J. Geophys. Res.-Space, 127, e2022JA030798, https://doi.org/10.1029/2022JA030798, 2022.

Nykiel, G., Cahuasquí, J. A., Hoque, M. M., and Jakowski, N.: Relationship between GIX, SIDX, and ROTI ionospheric indices and GNSS precise positioning results under geomagnetic storms, GPS Solut., 28, 69, https://doi.org/10.1007/s10291-023-01611-5, 2024.

Pi, X., Mannucci, A. J., Lindqwister, U. J., and Ho, C. M.: Monitoring of global ionospheric irregularities using the Worldwide GPS Network, Geophys. Res. Lett., 24, 2283–2286, https://doi.org/10.1029/97GL02273, 1997.

Rao, H., Chen, C., Meng, G., Liu, J., Sun, Y., Lin, K., Gao, Y., Rapoport, Y., Wang, F., Yisimayili, A., and Zhang, S.: Relationship Between TEC Perturbations and Rayleigh Waves Associated With 2023 Turkey Earthquake

Doublet, J. Geophys. Res.-Space, 130, e2024JA033267, https://doi.org/10.1029/2024JA033267, 2025.

Sheng, Z., He, Y., Wang, S., Chang, S., Leng, H., Wang, J., Zhang, J., Wang, Y., Zhang, H., Sui, H., Song, Y., Wu, G., Guo, S., Chai, J., Feng, W., and Song, J.: Dynamics, chemistry, and modelling studies in the aviation and aerospace transition zones, The Innovation, 6, 101012, https://doi.org/10.1016/j.xinn.2025.101012, 2025.

Snay, R. A. and Soler, T.: Continuously Operating Reference Station (CORS): History, Applications, and Future Enhancements, J. Surv. Eng., 134, 95–104, https://doi.org/10.1061/(ASCE)0733-9453(2008)134:4(95), 2008.

Song, X., Zhong, J., Hao, Y., Bai, T., Wan, X., Huang, F., Li, Q., Zhao, J., Han, H., Chen, J., and Lei, J.: Transition from westward to eastward tilts of equatorial plasma bubbles observed by an all-sky airglow imager, J. Space Weather Spac., 15, 38, https://doi.org/10.1051/swsc/2025032, 2025.

Takamatsu, N., Muramatsu, H., Abe, S., Hatanaka, Y., Furuya, T., Kakiage, Y., Ohashi, K., Kato, C., Ohno, K., and Kawamoto, S.: New GEONET analysis strategy at GSI: daily coordinates of over 1300 GNSS CORS in Japan throughout the last quarter century, Earth Planets Space, 75, 49, https://doi.org/10.1186/s40623-023-01787-7, 2023.

Wang, N., Yuan, Y., Li, Z., Montenbruck, O., and Tan, B.: Determination of differential code biases with multi-GNSS observations, J. Geodesy, 90, 209–228, https://doi.org/10.1007/s00190-015-0867-4, 2016.

Wang, N., Li, Y., Li, Z., Liu, A., and Liu, B.: Determination of multi-GNSS differential code biases with satellite antenna phase center corrections, GPS Solut., 30, 22, https://doi.org/10.1007/s10291-025-01983-w, 2026.

Woodgate, P., Coppa, I., Choy, S., Phinn, S., Arnold, L., and Duckham, M.: The Australian approach to geospatial capabilities; positioning, earth observation, infrastructure and analytics: issues, trends and perspectives, Geo-Spat. Inf. Sci., 20, 109–125, https://doi.org/10.1080/10095020.2017.1325612, 2017.

Yang, Y., Liu, L., Li, J., Yang, Y., Zhang, T., Mao, Y., Sun, B., and Ren, X.: Featured services and performance of BDS-3, Sci. Bull., 66, 2135–2143, https://doi.org/10.1016/j.scib.2021.06.013, 2021.

Yuan, Y., Wang, N., Li, Z., and Huo, X.: The BeiDou global broadcast ionospheric delay correction model (BDGIM) and its preliminary performance evaluation results, Navigation, 66, 55–69, https://doi.org/10.1002/navi.292, 2019.

Zhai, C., Zhang, S., Yao, Y., Dong, W., Aa, E., Kong, J., Yue, D., Chen, Y., Peng, W., and Yu, T.: Three-Dimensional Characterization of Global Ionospheric Disturbances During the 15 January 2022 Tonga Volcanic Eruption, Geophys. Res. Lett., 52, e2024GL113129, https://doi.org/10.1029/2024GL113129, 2025.

Zhang, R., Liu, L., Yang, Y., Li, W., Zhao, X., Yoshikawa, A., Tariq, M. A., Chen, Y., and Le, H.: Ionosphere Responses Over Asian-Australian and American Sectors to the 10–12 May 2024 Superstorm, J. Geophys. Res.-Space, 129, e2024JA033071, https://doi.org/10.1029/2024JA033071, 2024.

Zhang, Z., Wang, N., Liu, A., Li, Z., Li, A., Wang, L., and Zhang, Y.: Assessing 1-Second ROTI for Ionospheric Perturbation Monitoring Using Real-Time Multi-GNSS Data in China, Space Weather, 23, e2024SW004187, https://doi.org/10.1029/2024SW004187, 2025.

Zhong, J., Lei, J., Dou, X., and Yue, X.: Assessment of vertical TEC mapping functions for space-based GNSS observations, GPS Solut., 20, 353–362, https://doi.org/10.1007/s10291-015-0444-6, 2016a.

Zhong, J., Lei, J., Dou, X., and Yue, X.: Is the long-term variation of the estimated GPS differential code biases associated with ionospheric variability?, GPS Solut., 20, 313–319, https://doi.org/10.1007/s10291-015-0437-5, 2016b.

Zhong, J., Han, H., Hao, Y., Wan, X., Huang, F., Li, Q., Song, X., Chen, J., and Lei, J.: Accurate Estimation of Height and Zonal Drift Velocity of Ionospheric Irregularities Using Two Pairs of Receivers and BeiDou Geostationary Satellites, IEEE T. Geosci. Remote, 61, 1–10, https://doi.org/10.1109/TGRS.2023.3326441, 2023.